The Analysis of In-Membrane Nanoscopic Aggregation of Lipids and Proteins by MC-FRET

Barbora Chmelová, Jana Humpolíčková, Kvido Stříšovský, and Radek Šachl

Contents

Abstract Many lipids and membrane proteins spontaneously co-cluster and oligomerize in cellular plasma membranes into larger (functional) units, whose detailed characterization requires high spatial resolution. In this contribution, we introduce a powerful spectroscopy/microscopy approach called MC-FRET

Barbora Chmelová and Jana Humpolíčková contributed equally to this work.

B. Chmelová
J. Heyrovský Institute of Physical Chemistry of the Academy of Sciences of the Czech Republic, Prague, Czech Republic

Faculty of Mathematics and Physics, Charles University, Prague, Czech Republic
e-mail: barbora.chmelova@jh-inst.cas.cz

J. Humpolíčková and K. Stříšovský
Institute of Organic Chemistry and Biochemistry of the Academy of Sciences of the Czech Republic, Prague, Czech Republic
e-mail: jana.humpolickova@uochb.cas.cz; kvido.strisovsky@uochb.cas.cz

R. Šachl (✉)
J. Heyrovský Institute of Physical Chemistry of the Academy of Sciences of the Czech Republic, Prague, Czech Republic
e-mail: radek.sachl@jh-inst.cas.cz

R. Šachl, M. Amaro (eds.), *Fluorescence Spectroscopy and Microscopy in Biology*, Springer Ser Fluoresc (2023) 20: 375–400, https://doi.org/10.1007/4243_2022_29,
Published online: 4 August 2022

developed for the analysis of in-membrane nanoscopic aggregation of lipids and proteins in biological membranes. The approach is based on Förster resonance energy transfer (FRET) occurring in membranes between fluorescently labelled lipids/proteins and subsequent analysis of data by Monte-Carlo simulations. The following applications of MC-FRET are presented here: (1) determination of lipid nanodomain sizes and their surface density; (2) characterization of inter-leaflet organization of lipid nanodomains and (3) the analysis of dimerization of in-membrane proteins.

Keywords Dimers · FRET · Gangliosides · GPMVs · Kappa squared · MC-FRET · Membrane protein–protein interactions · Nanodomains · Oligomerization

Abbreviations

A	Acceptor
ACF	Autocorrelation function
B.-F.	Bauman-Fayer model
bSM	Brain sphingomyelin
C	Surface concentration
CF-PEG-DSPE	Carboxyfluorescein-2-distearoyl-sn-glycero-3-phosphoethanolamine-*N*-[amino (Polyethylene glycol) 2000]
CTxB	Cholera toxin β
D	Donor
d	The distance between two bilayer leaflets
DGS-NTA(Ni)	1,2-Dioleoyl-sn-glycero-3-[(*N*-(5-amino-1-carboxypentyl) iminodiacetic acid)succinyl]
DHE	Dehydroergosterol
DHPE FITC	Fluorescein dihexadecanoylphosphatidylethanolamine
DHPE TR	Texas red dihexadecanoylphosphatidylethanolamine
DiI	1,1'-Dioctadecyl-3,3,3',3'-tetramethylindocarbocyanine perchlorate
DiOC18	Dioctadecyloxacarbocyanine perchlorate
DLPC	Dilauroylphosphatidylcholine
DOPC	1,2-Dioleoyl-sn-glycero-3-phosphocholine
DOPG	1,2-Dioleoyl-sn-glycero-3-phospho-glycerol
DPhPC	Diphytanoylphosphatidylcholine
DSPC	1,2-Distearoyl-sn-glycero-3-phos-phocholine
DSPC	Distearoylphosphatidylcholine
FCCS	Fluorescence cross-correlation spectroscopy
FP	Fused proteins
FRET	Förster resonance energy transfer
GCPII	Glutamate carboxypeptidase II
g-GM_1	Ganglioside GM_1 labelled in the headgroup with FL-BODIPY

G_i(t)	Survival probability function
GPMVs	Giant plasma membrane vesicles
GUVs	Giant unilamellar vesicles
GWALP23	Acetyl-GGALW^{5}LAL^{8}ALALALAL^{16}ALW^{19}LAGA-amide
iSCAT	Interferometric scattering microscopy
κ^2	Kappa squared
K_d	Dissociation constant
K_D	Distribution constant
L_0	The closest protein–protein distance
MC-FRET	FRET analysed by Monte-Carlo simulations
MSD	Mean square displacement
N_A	Numerical aperture
NBD-DLPE	*N*-(7-nitrobenz-2-oxa-1,3-diazol-4-yl)-dilauroylphosphatidylethanolamine
PALM	Photo-activated localization microscopy
PGPC	1-Palmitoyl-2-glutaryl-*sn*-glycero-3-phosphocholine
PIP2	Phosphatidylinositol 2
POPC	Palmitoyl-oleoyl-phosphocholine
POVPC	1-Palmitoyl-2-(5′-oxo-valeroyl)-*sn*-glycero-3-phosphocholine
PSM	Palmitoyl-sphingomyelin
Q_{DA}/Q_D	Quantum yield in the presence/absence of acceptors
R_0	Förster radius
r-GM_1	Ganglioside GM_1 labelled in the headgroup with 564/570-BODIPY
Rh-PEG-DSPE	Rhodamine101–2-distearoyl-*sn*-glycero-3-phosphoethanolamine-*N*-[amino (Polyethyleneglycol) 2000]
SM	Sphingomyelin
STED	Stimulated emission depletion microscopy
TCSPC	Time-correlated single photon counting
TOE	Tryptophan oleoyl ester
TRF	Time-resolved fluorescence
η	FRET efficiency

1 Introduction

Biophysical experiments performed in the last decades have shown that nanoscale distribution of lipids and proteins in cellular membranes is rather complicated and far from being completely homogeneous (see, for instance, the following reviews) [1, 2]. On the contrary, many lipids and membrane proteins spontaneously co-cluster and oligomerize into larger functional units, which may be essential for proper functioning of biological membranes [2]. To give a few examples for all, gangliosides self-assemble in plasma membranes into several tens of nanometre

large lipid nanodomains, forming a platform for ligand to receptor interactions [3, 4]. Similarly, phosphatidylinositol-bisphosphates (PIP2), involved in cellular signalling, also co-cluster and form nanoscopic domains [5, 6]. Or, interestingly, trans-membrane proteins engaged in the respiratory chain cycle oligomerize into huge super-molecular complexes, which seem important for the proper function of the respiratory chain cycle [7].

These findings were achieved by the rapid development of advanced biophysical approaches that can detect and characterize nanoscopic objects in the membrane by offering high spatial and temporal resolution. These high-resolution approaches undoubtedly include fluorescence techniques such as Förster Resonance Energy Transfer (FRET) [8], Photo-Activated Localization Microscopy (PALM) [9], Stochastic Optical Reconstruction Microscopy [10] or Stimulated Emission Depletion Microscopy (STED) [11], but also label-free techniques such as Interferometric SCATtering microscopy (iSCAT) [12, 13], X-ray, neutron scattering, electron or atomic force microscopy and others [14, 15]. Whereas most of the above-mentioned fluorescence techniques are reviewed in other chapters of this book, this chapter focuses on the applications of FRET in the analysis of lipid nanodomain formation and in-membrane oligomerization of proteins.

The approach is based on the use of lipids and proteins that are labelled by either fluorescence donors or acceptors and the fact that their self-assembly will change the originally homogeneous donor and acceptor distributions into heterogeneous ones, bringing the donors closer to the acceptors, or taking them apart (Fig. 1). As a result, the efficiency of FRET will either increase or decrease, which can be quantified by either measuring the fluorescence intensity of the donors, or more precisely, their corresponding time-resolved fluorescence (TRF) decays. The analysis of TRF data by a novel analytical approach called MC-FRET [16, 17] (FRET analysed by Monte-Carlo simulations) enables then to measure lipid nanodomain sizes with nanometre precision, or, in case of protein oligomerization, to characterize the oligomeric state.

The structure of this chapter is as follows: we first review the classical analytical model that is used to analyse FRET between donors and acceptors that are homogeneously distributed in lipid bilayers (Sect. 2), introduce the MC-FRET approach developed for the analysis of FRET between heterogeneously distributed probes where analytical approaches fail (Sect. 3.1) and then describe the following applications of MC-FRET: (1) estimation of lipid nanodomain sizes and their surface density (Sect. 3.2), (2) discrimination between inter-leaflet coupled and inter-leaflet independent or anti-registered nanodomains (Sect. 3.3) and (3) quantification of protein dimerization in the native membrane (Sect. 3.4). Overall, a careful analysis of this approach reveals that MC-FRET can detect nanodomains as small as a few nanometres and determine whether the nanodomains are inter-leaflet coupled or independent [18]. Moreover, FRET allows for quantitative description of protein–protein interactions in planar lipid bilayers. The conclusions drawn in the following quantitative studies [19–21] specify in detail the facts that have to be considered when studying protein dimerization in non-planar membranes, such as Golgi, for example.

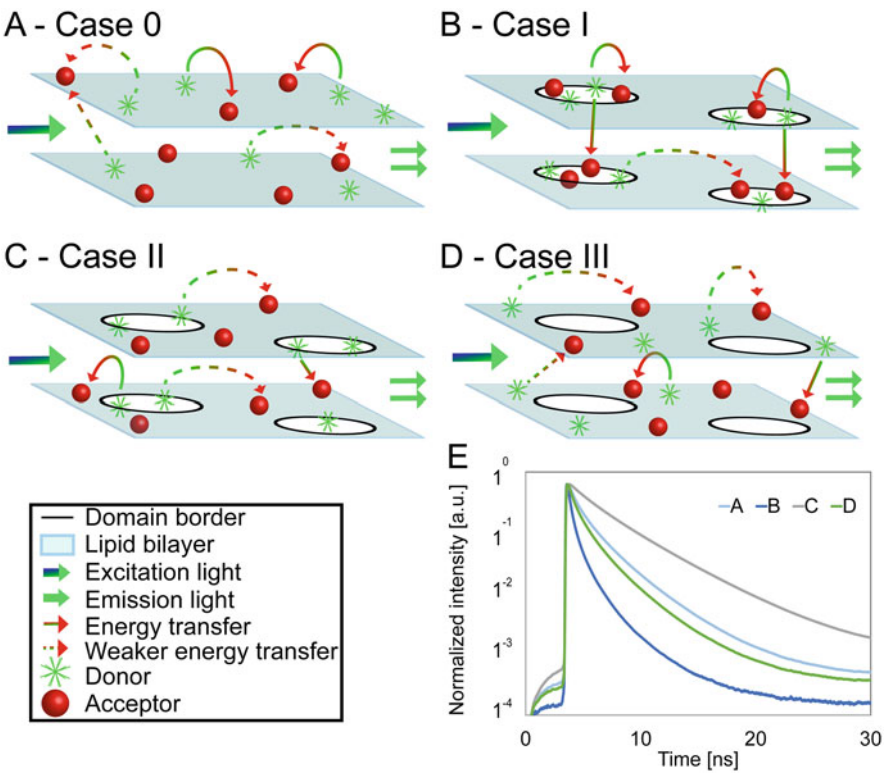

Fig. 1 (**a**–**d**) Possible arrangements of donors and acceptors in respect of the nanodomains and (**e**) corresponding time-resolved fluorescence decays of donors in the presence of acceptors. (**a**) A nanoscopically homogeneous bilayer with randomly distributed donors and acceptors; (**b**–**d**) A nanoscopically heterogeneous bilayer with (**b**) both donors and acceptors exhibiting increased affinity to the nanodomains; (**c**) donors localized in the nanodomains and acceptors excluded from them and (**d**) both donors and acceptors excluded from the nanodomains

2 FRET Between Homogeneously Distributed Donors and Acceptors

A cellular plasma membrane approximated by a lipid bilayer consists of two parallel sheets. Under the assumption that each leaflet contains homogeneously distributed donors and acceptors, FRET will occur both within one leaflet and between the two leaflets at the same time (Fig. 1). Whereas the first process is referred to as *intra*-FRET and depends only on the surface concentration of acceptors, the latter one is known as *inter*-FRET and depends in addition on the distance between the two bilayer leaflets d. In the absence of FRET, the donor fluorescence intensity $F_D(t)$ can be expressed as:

$$F_{\mathrm{D}}(t) = \sum_i \alpha_i \exp\left(-\frac{t}{\tau_i}\right). \tag{1}$$

Here, α_i denotes the preexponential factors and τ_i the corresponding fluorescence lifetimes. To express mathematically the kinetics of fluorescence deexcitation of the donors in the presence of acceptors, it is convenient to introduce a so-called survival probability function $G(t)$ describing the probability that a donor is still found in the excited state at the time t after the excitation. When several independent deexcitation processes occur at the same time, the total probability function $G_{\mathrm{TOT}}(t)$ equals the product of $G_{\mathrm{i}}(t)$ functions for individual deexcitation processes:

$$G_{\mathrm{TOT}}(t) = \prod G_i(t). \tag{2}$$

By assuming dynamic limit conditions, where movements of dipoles are much faster than an energy transfer event, Bauman and Fayer showed that $G(t)$ for *intra*-FRET, G_{intra} [22], equals

$$\ln G_{\mathrm{intra}}(t) = -C_2\Gamma\left(\frac{2}{3}\right)\left(\frac{t}{\langle\tau_{\mathrm{D}}\rangle}\right)^{1/3}. \tag{3}$$

Here, Γ denotes the gamma function, $\langle\tau_{\mathrm{D}}\rangle$ the intensity averaged fluorescence lifetime of donors in the absence of acceptors and C_2 the reduced surface concentration of acceptors in one leaflet. This concentration represents the average number of acceptors within the area of πR_0^2 and is related to the acceptor surface concentration $C(\mathrm{A})$ by: $C_2 = \pi R_0^2 C(\mathrm{A})$. In the same work, the authors derived $G(t)$ for *inter*-FRET, $G_{\mathrm{inter}}(t)$ [22].

$$\ln G_{\mathrm{inter}}(t) = -\frac{C_2}{3}\left(\frac{d}{R_0}\right)^2\left(\frac{2\mu}{3}\right)^{1/3}\int_0^{2/3\mu}(1-e^{-s})s^{-4/3}ds, \tag{4}$$

where θ_r is the angle between the bilayer normal and the vector connecting the locations of the donor and acceptor dipoles, $\mu = 3t\left(\frac{R_0}{d}\right)^6\frac{1}{2\langle\tau\rangle}$ and $s = 2\mu\cos^6\frac{\theta_r}{3}$. As a result, the kinetics of fluorescence deexcitation of the donors in the presence of acceptors, $F_{\mathrm{DA}}(t)$, can be expressed for the classical case where both donors and acceptors are localized in the lipid bilayer at the same distance from the lipid–water interface as

$$F_{\mathrm{DA}}(t) = G_{\mathrm{intra}}(t)G_{\mathrm{inter}}(t)F_{\mathrm{D}}(t). \tag{5}$$

Fitting time-resolved fluorescence data by this equation enables to transversely localize fluorescent probes with subnanometre resolution and to accurately determine the surface concentration of acceptors [23].

3 FRET Between Heterogeneously Distributed Donors and Acceptors

3.1 Heterogeneous Probe Distributions Induced by Lipid Nanodomain Formation or Protein Oligomerization

Heterogeneous probe distribution can arise in lipid bilayers in two different ways: (1) either due to formation of membrane lipid nanodomains to which donors and/or acceptors have different affinity in comparison with the surrounding nondomain phase (Sects. 3.2 and 3.3) [16] or (2) because of co-clustering of the donors with the acceptors (Sect. 3.4). Both cases result in each donor having a different radial distribution of acceptors around itself, which makes it difficult to derive precise mathematical formulas describing FRET in such a heterogeneous probe environment. As will be shown below, this limitation can be effectively circumvented by analysing FRET using MC simulations, giving rise to a new analytical approach called MC-FRET. In this approach, MC simulations are used to mimic FRET in the heterogeneous probe environment and to generate in-silico TRF decay curves that are compared to the experimental ones in an iterative fashion (Sect. 3.2.1), enabling to study formation of membrane nanodomains [8, 24] (Sects. 3.2 and 3.3), or in-membrane oligomerization of proteins (Sect. 3.4).

3.2 The Estimation of Lipid Nanodomain Sizes by MC-FRET

To characterize membrane lipid nanodomains by MC-FRET, the used donor and acceptor probes need to exhibit a distinct affinity to the nanodomains and the region outside of them. In such case, the shape of TRF decays of the donors in the presence of acceptors will be influenced by the size, surface density and inter-leaflet organization of the nanodomains. All of these parameters can be estimated by MC-FRET [17].

To characterize the probe affinity towards nanodomains it is convenient to introduce a distribution constant for donors, $K_D(D)$, or acceptors, $K_D(A)$, as $K_D(D/A) = C(D/A \text{ inside of a domain})/C(D/A \text{ outside of a domain})$ between the nanodomains and the region outside of them with the help of donor/acceptor surface concentrations inside (C(D/A inside)) or outside (C(D/A inside)) of the nanodomains, respectively. The following situations may arise: Case 0): $K_D(D) = 1$ and $K_D(A) = 1$. Consequently, the probes are distributed homogenously across the entire lipid bilayer regardless of the presence of nanodomains (Fig. 1a). Such a situation does not allow for the detection of nanodomains using MC-FRET. Case I) $K_D(D) > 1$ and $K_D(A) > 1$, implying that both donors and acceptors accumulate inside of the nanodomains (Fig. 1b). Such a spatial accumulation of the probes decreases the average distance between the probes and leads to enhanced FRET efficiency and faster relaxation of donors into the ground state (Fig. 1e) as compared

to the homogeneous probe distribution (Case 0, Fig. 1a). Case II) $K_D(D) > 1$ and $K_D(A) < 1$ or $K_D(D) < 1$ and $K_D(A) > 1$, which results in the accumulation of donors and acceptors in distinct bilayer regions, and consequently spatial separation of donors from acceptors (Fig. 1c). Such a probe distribution yields a lower FRET efficiency and slower relaxation kinetics in comparison with Case 0 (Fig. 1e). And finally, Case III) $K_D(D) < 1$ and $K_D(A) < 1$. Since both donors and acceptors are excluded from nanodomains in this case, the efficiency of FRET will be increased, and the relaxation kinetics accelerated in comparison with homogenous probe distribution.

3.2.1 Workflow of MC-FRET for the Nanoscopic Characterization of Nanodomains

The MC-FRET analysis is based on fitting experimental TRF decays by the decays generated by MC simulations and follows the basic scheme depicted in Fig. 2. The entire procedure starts by generation of a defined number of nanodomains on the bilayer surface. The nanodomains are assumed to be circular in shape, uniform in size, perfectly registered across the two bilayer leaflets and are characterized by the nanodomain radius, $\langle R \rangle$, and their surface density, $\langle A \rangle$. In the next step, donors and acceptors are distributed between the nanodomains and the remaining bilayer part according to their $K_D(D)$ and $K_D(A)$. The total number of acceptors that enters the simulation is estimated on the same sample prior to nanodomain formation by FRET (see the Baumann-Fayer model (B.-F.) presented in Sect. 2). Then, a donor is randomly excited, and the time Δt_i at which energy transfer takes place calculated according to $\Delta t_i = -\ln \gamma / \Omega_i$, where γ is a randomly generated number between 0–1 and Ω_i is the overall energy transfer rate.

In the case of a randomly excited donor in the presence of multiple acceptors, Ω_i can be expressed as the sum of the rates between the donor and each of the acceptors:

$$\Omega_i = \frac{1}{\langle \tau_D \rangle} \sum_j \left(\frac{R_0}{R_j} \right)^6 . \tag{6}$$

Here, j goes through all acceptors in the system and R_0 stands for the Förster radius. For the sake of simplicity, the distance R_j between the i-th selected donor and the acceptors is evaluated only for the acceptors that are closer than the cut-off distance R_c ($10R_0$); the acceptors behind that cut-off are treated as a continuum:

$$\Omega_i = \frac{1}{\langle \tau_D \rangle} \left(\sum_j \left(\frac{R_0}{R_j} \right)^6 + 0.5 \times C_2 \times \left(\frac{R_0}{R_c} \right)^4 \right), \text{for } j, \text{where } |R_i - R_j| \leq 10R_0. \tag{7}$$

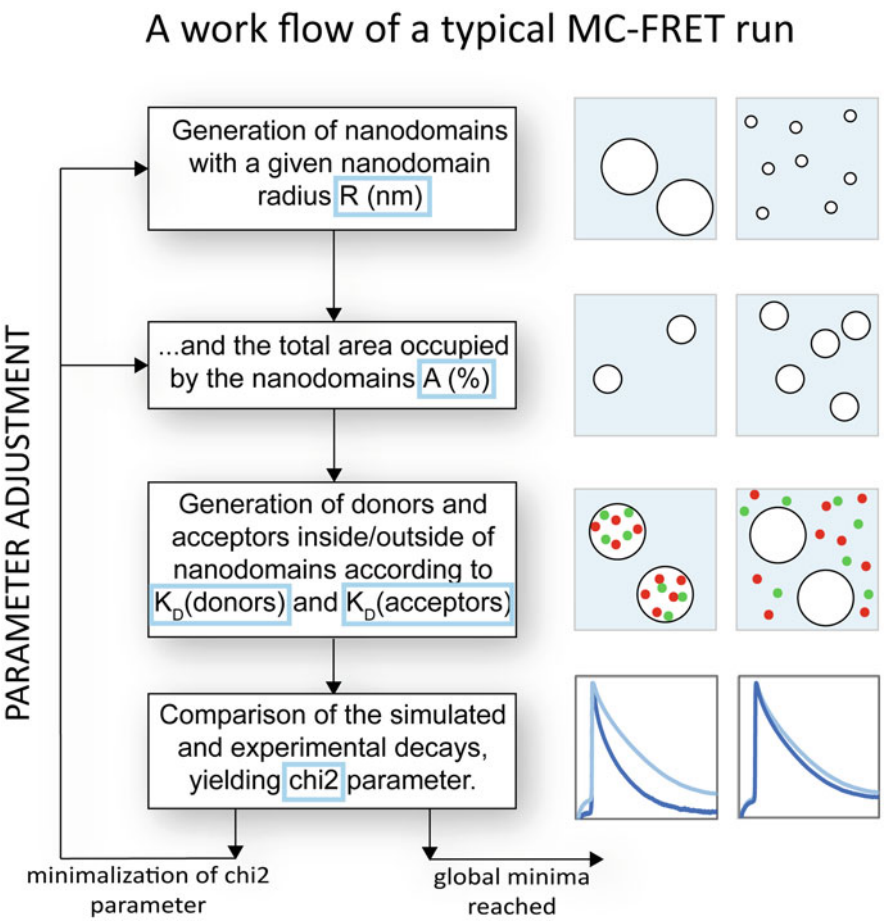

Fig. 2 A workflow of an MC-FRET simulation yielding the optimized nanodomain radius, the total area occupied by the nanodomains and optionally the distribution constants $K_D(D)$, $K_D(A)$

The outcome of each simulation step is the time interval Δt_i between the excitation and energy transfer event. By constructing a histogram of Δt_i intervals, the total survival probability function $G_{TOT}(t)$ is obtained, and the simulated decay of the donors quenched by the acceptors $F_{DA}(t)$ calculated $F_{DA}(t) = G_{TOT}(t)F_D(t)$. The simulated decay is fitted to the experimental one by varying the input simulation parameters, i.e., the domain radius $\langle R \rangle$, the area fraction occupied by the domains $\langle A \rangle$, and K_D(D/A).

3.2.2 What Nanodomain Sizes Can Be Resolved by MC-FRET? [18]

Nanodomains can be detected by MC-FRET only if their formation influences the shape of TRF decays of the donors quenched by acceptors. Thus, to characterize the resolution of MC-FRET it is convenient to introduce a parameter *RES*, defined as

$$\mathrm{RES} = \frac{1}{n}\sum_{i=1}^{n}\frac{\mathrm{abs}(F_{\mathrm{DA,homo}}(t_i) - F_{\mathrm{DA,hetero}}(t_i))}{F_{\mathrm{DA,homo}}(t_i)}100. \tag{8}$$

This parameter quantifies the difference between the TRF decay recorded in the absence of nanodomains, $F_{\mathrm{DA,\ homo}}(t_i)$, where probes are distributed homogeneously, and the decay recorded in the presence of nanodomains, $F_{\mathrm{DA,\ hetero}}(t_i)$, where, in contrast, the probes are distributed heterogeneously. With the help of this parameter, the resolution of MC-FRET can be characterized as follows: (1) $RES \leq 10\%$ (red colour on the colormap bar of Fig. 3), yielding very similar TRF decays for the homogeneous and heterogeneous probe distributions. At the same time, this parameter value corresponds to the change in the steady-state intensity of donors, $\langle F_{\mathrm{DA,\ hetero}}\rangle/\langle F_{\mathrm{DA,\ homo}}\rangle$, and the average fluorescence lifetime, $\langle \tau_{\mathrm{DA,\ hetero}}\rangle/\langle \tau_{\mathrm{DA,\ homo}}\rangle$, of less than 10%. Such conditions are unfavourable for the characterization of nanodomains by MC-FRET. (2) $RES \in (10; 20)\%$ (yellow colour on the colormap bar of Fig. 3), enabling the detection of nanodomains by MC-FRET. This parameter value is accompanied by the change in $\langle F_{\mathrm{DA,\ hetero}}\rangle/\langle F_{\mathrm{DA,\ homo}}\rangle$ by more than 10% and the change in $\langle \tau_{\mathrm{DA,\ hetero}}\rangle/\langle \tau_{\mathrm{DA,\ homo}}\rangle$ that does not exceed 10%. (3) $RES \in (20; 30\rangle\%$ (green colour on the colormap bar of Fig. 3), yielding clearly distinct TRF decays. This parameter value results in the change of $\langle F_{\mathrm{DA,\ hetero}}\rangle/\langle F_{\mathrm{DA,\ homo}}\rangle$ of up to 20% and the change in $\langle \tau_{\mathrm{DA,\ hetero}}\rangle/\langle \tau_{\mathrm{DA,\ homo}}\rangle$ that is above 10%. (4) $RES \in (30; 60\rangle\%$ (cyan colour on the colourmap bar of Fig. 3), leading to the change in $\langle F_{\mathrm{DA,\ hetero}}\rangle/\langle F_{\mathrm{DA,\ homo}}\rangle$ of up to 40% and the change in $\langle \tau_{\mathrm{DA,\ hetero}}\rangle/\langle \tau_{\mathrm{DA,\ homo}}\rangle$ of more 10%. (5) Finally, if $RES > 60\%$ (blue colour on the colormap bar of Fig. 3), $\langle F_{\mathrm{DA,\ hetero}}\rangle/\langle F_{\mathrm{DA,\ homo}}\rangle > 30\%$ and $\langle \tau_{\mathrm{DA,\ hetero}}\rangle/\langle \tau_{\mathrm{DA,\ homo}}\rangle > 20\%$.

To calculate the parameter *RES* by Eq. (8), we generated the TRF decays for the homogeneous, $F_{\mathrm{DA,\ homo}}(t_i)$, and heterogeneous, $F_{\mathrm{DA,\ hetero}}(t_i)$, probe distributions assuming various $\langle R\rangle$, $\langle A\rangle$, K_{D}(D) and K_{D}(A). The parameter *RES* is plotted for Cases I, II and III as a function of $\langle R\rangle$ and $\langle A\rangle$ in Fig. 3. A careful inspection of the figure reveals that in case of an extremely high probe affinity to either the nanodomains or the region outside of them (characterized by $K_{\mathrm{D}}(\mathrm{D/A}) = 1000$ or $K_{\mathrm{D}}(\mathrm{D/A}) = 1/1000$) the resolution of MC-FRET is excellent for most combinations of $\langle R\rangle$ and $\langle A\rangle$. An exception represents a relatively narrow region defined by $\langle R\rangle \in \langle 5; 20\rangle$ nm and $\langle A\rangle \in \langle 1; 15\rangle$ % for $K_{\mathrm{D}}(\mathrm{D/A}) = 0.001$. To identify the Case that provides the best resolution, we generated the diagrams for $K_{\mathrm{D}}(\mathrm{D/A}) = 10$ or $K_{\mathrm{D}}(\mathrm{D/A}) = 1/10$, respectively (Fig. 3). Based on this comparison, Case II ($K_{\mathrm{D}}(\mathrm{D}) > 1$ and $K_{\mathrm{D}}(\mathrm{A}) < 1$) performs the best, followed by Case I ($K_{\mathrm{D}}(\mathrm{D}) > 1$ and $K_{\mathrm{D}}(\mathrm{A}) > 1$), whereas Case II ($K_{\mathrm{D}}(\mathrm{D}) < 1$ and $K_{\mathrm{D}}(\mathrm{A}) < 1$) performs the worst. Most important of all, even such low and physically realistic K_{D}(D/A) values provide sufficient

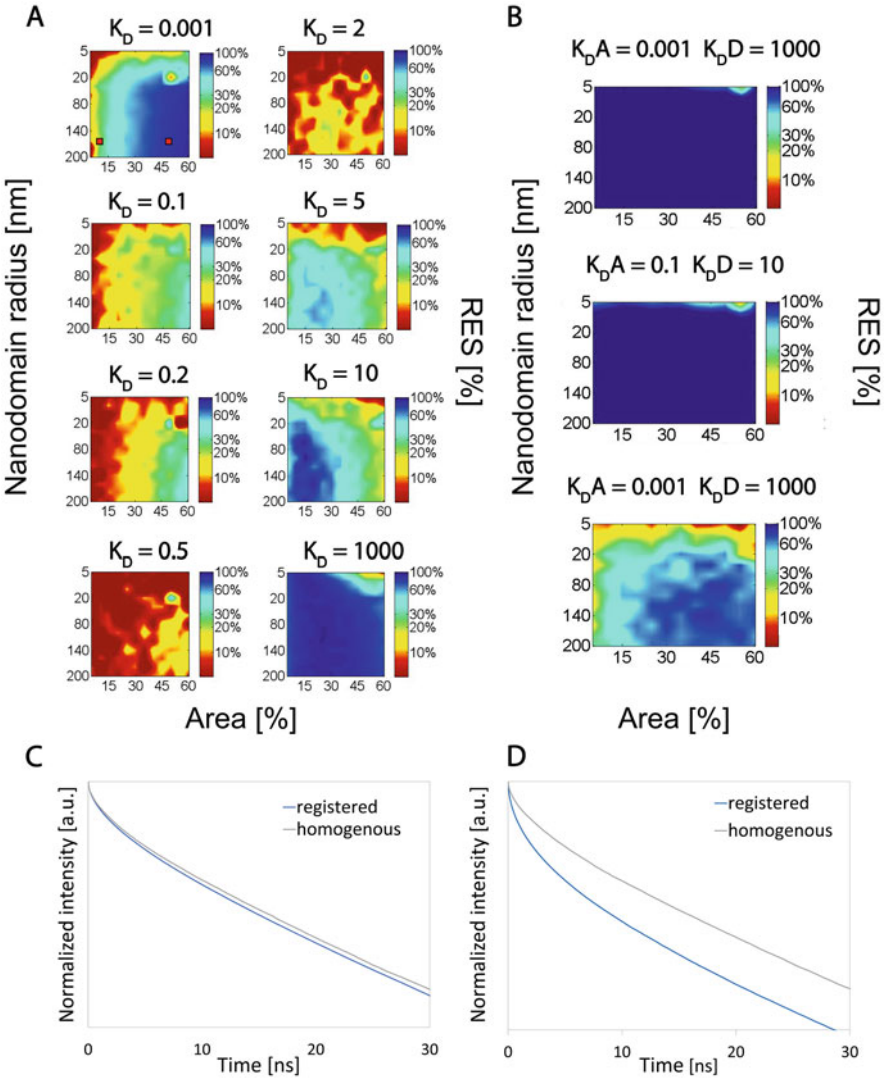

Fig. 3 The resolution of MC-FRET in the detection of membrane nanodomains as a function of the nanodomain radius and the fractional area occupied by the nanodomains shown for various K_Ds. The resolution is characterized by the parameter RES defined in the text. (**a**) $K_D(D) = K_D(A)$, (**b**) $K_D(D) \geq 1$ and $K_D(A) \leq 1$. (**c**, **d**) Time-resolved fluorescence decays for a homogeneous bilayer and the bilayer containing registered nanodomains characterized by RES = 19.5% (**c**) and RES = 83.8% (**d**). The decays were extracted from the positions in the resolution diagram depicted by solid red squares

resolution for all cases. Although by approaching the K_D(D/A) values even closer to one (K_D(D/A) = 2 or K_D(D/A) = 1/2) the resolution of MC-FRET continues to decline significantly (Fig. 3), Case III still offers a satisfactory resolution as opposed to Cases I and II.

Overall, the results presented so far show that choosing the right donor–acceptor pair is essential to achieve the best possible resolution. Therefore, we compiled a table that summarizes such donor–acceptor pairs, which, to the best of our knowledge, have so far been used in the detection and characterization of both micro- and nanodomains of different features (Table 1). It follows from the table that although there exist enough fluorescent probes that spontaneously localize both inside and outside the domains, fluorescent probes having a considerable affinity for the domains ($K_D \geq 10$) are essentially non-existent. According to our knowledge, the highest affinity exhibits headgroup-labelled gangliosides ($K_D \geq 20$) frequently used in our laboratory [8, 17, 25] or tryptophan labelled peptide GWALP23 ($K_D = 13$) [26]. On the contrary, plenty of probes excluded from the domains are available (Table 1). Most importantly, probes that have a modest affinity for the domains ($K_D \approx 10$) or the region outside them ($K_D \approx 0.1$) are sufficient for MC-FRET, and a satisfactory number of such probes have been characterized so far (Table 1).

3.3 Resolving Inter-Leaflet Coupled from Inter-Leaflet Independent Nanodomains by MC-FRET

Thanks to energy transfer that occurs not only within one bilayer leaflet but also from one leaflet to the other one, the measured FRET efficiency will also depend on the mutual organization of the nanodomains in the lower and upper leaflets [36]. Thus, MC-FRET, in contrast to other fluorescence approaches, offers excellent axial resolution and can be used to study inter-leaflet organization of nanodomains [17]. In principle, the following scenarios may arise (Fig. 4): (1) Nanodomains are perfectly registered across the bilayer leaflets (Fig. 4a), (2) the nanodomains in the upper and lower leaflets are independent from each other (Fig. 4b) and (3) nanodomains are anti-registered (Fig. 4c). In this case, the nanodomains in the two leaflets avoid each other, and thus, the nanodomains in the upper leaflet cannot occupy the lateral positions that have already been taken by the nanodomains in the lower leaflet, and vice versa. To identify the most likely scenario, the experimental TRF decays are fitted by the decays generated for the scenarios 1–3. As the most probable is classified the scenario that provides the best fit and the lowest value of the chi2 parameter. Since the resolution of MC-FRET depends significantly on the extent to which the decays for scenarios 1–3 differ, it can again be characterized by means of the parameter RES. The parameter, however, is now defined as

Table 1 The affinity of selected donor–acceptor pairs to various types of membrane lipid domains characterized by their K_D's, defined as $K_D(D/A) = C(D/A \text{ inside of a domain})/C(D/A \text{ outside of a domain})$

D	A	$K_D(D)$	$K_D(A)$	Lipid composition	R_0 (nm)	Domain phase	Reference
NBD-DLPE	DiIC12(3)	0.21	0.11	DLPC/DSPC (60:40)	5.2	Gel phase nanodomains	[27]
NBD-DLPE	DiIC12(3)	0.41	0.14	DLPC/DSPC (40:60)	5.2		
NBD-DLPE	DiIC18(3)	0.21	0.15	DLPC/DSPC (60:40)	5.2		
NBD-DLPE	DiIC18(3)	0.41	0.15	DLPC/DSPC (40:60)	5.2		
DHE	DiOC18 saturated	0.61± 0.02	7.4± 0.2	DLPC/DPPC (25:75)	5	Nanodomains of fluid and solid phases	[28]
DiOC18 saturated	DiIC18 unsaturated	7.4± 0.2	0.22± 0.01	DLPC/DPPC (25:75)	4.2 [29]		
DiOC18 saturated	DiIC18 saturated	7.4± 0.2	7.5± 0.3	DLPC/DPPC (25:75)	4.2 [29]		
DiOC18 unsaturated	DiIC18 saturated	0.23± 0.1	7.5± 0.3	DLPC/DPPC (25:75)	4.2 [29]		
NBD-DPPE	Rh-DOPE	3.68 ± 0.55	0.28± 0.08	POPC/PSM/Chol (33:33:33)	2.5/ 2.9Ld/ lo	Nanodomains with L_o character	[30]
TOE	DHE	0.11± 0.025	2.56	DSPC/DOPC/Chol (40/40/20)	2.4	Microdomains with L_o and L_d characters	[31]
TOE	DHE	0.1± 0.01	3.7	bSM/DOPC/Chol (40/40/20)	2.4		
DHE	Bodipy PC	2.56	0.09± 0.015	DSPC/DOPC/Chol (40/40/20)	2.8		
DHE	Bodipy PC	3.7	0.16± 0.025	bSM/DOPC/POPC/Chol (40/40/ 20)	2.8		
TOE	Bodipy PC	0.14± 0.025	0.1± 0.01	DSPC/DOPC/Chol (40/40/20)	2.5		

(continued)

Table 1 (continued)

D	A	K_D(D)	K_D(A)	Lipid composition	R_0 (nm)	Domain phase	Reference
TOE	Bodipy PC	0.12± 0.015	0.11± 0.025	bSM/DOPC/Chol (40/40/20)	2.5		
g-GM_1	r-GM_1	≥20	≥20	DOPC/Chol/SM (65–70/25/5–10)	5.87	Nanodomains with L_d character	[8]
g-GM_1	r-GM_1	10	10	DOPC/SM (85–90/10–15)	5.87		
CF-PEG-DSPE	Rh-PEG-DSPE	5	5	DOPC/Chol/SM (65/25/10)	6.63 [17]		
NBD-PE	Rh-PE	4.3	0.37	POPC/SM/Chol (33:33:33)	5	Nanodomains with L_o character	[18]
BODIPY-PC	Fast-DiI	0.1	0.1	DOPC/DSPC/Chol (30/30/40)	6.5		
DHPE-FITC	DHPE-TR	0.28	<<1	DPhPC/DPPC/Chol (40:35:25)		Nanodomains with L_o character	[32]
DHPE-OG488	DHPE-TR	2.1	<<1				
DHPE-NBD	DHPE-TR	2.2	<<1				
CTxB Alexa 488	DiD	6 ± 3	0.004 ± 0.002	DOPC/SM/Chol/DOPG/GM_1 (23–68/0–45/25/5/2)	5.4	Nanodomains with L_o character	[33]
NBD-PE	Rh-PE	4.3 ± 1.2	0.37 ± 0.06	PSM/POPC/Chol (33:33:33)	6.41	Nanodomains with L_o character	[34]
GWALP23 tryptophan	DHE	13 ± 2	Cca 1	DSPC/DOPC/Chol	6	Nanodomains with L_o and L_d characters	[35]
GWALP23 tryptophan	DHE	8 ± 1	Cca 1	bSM/DOPC/Chol	6		
NBD-cholesterol	Octadecyl rh-B	0.32	0.057	DMPC/Chol (80/20)	4.48	Microdomains with L_o and L_d characters	[26]

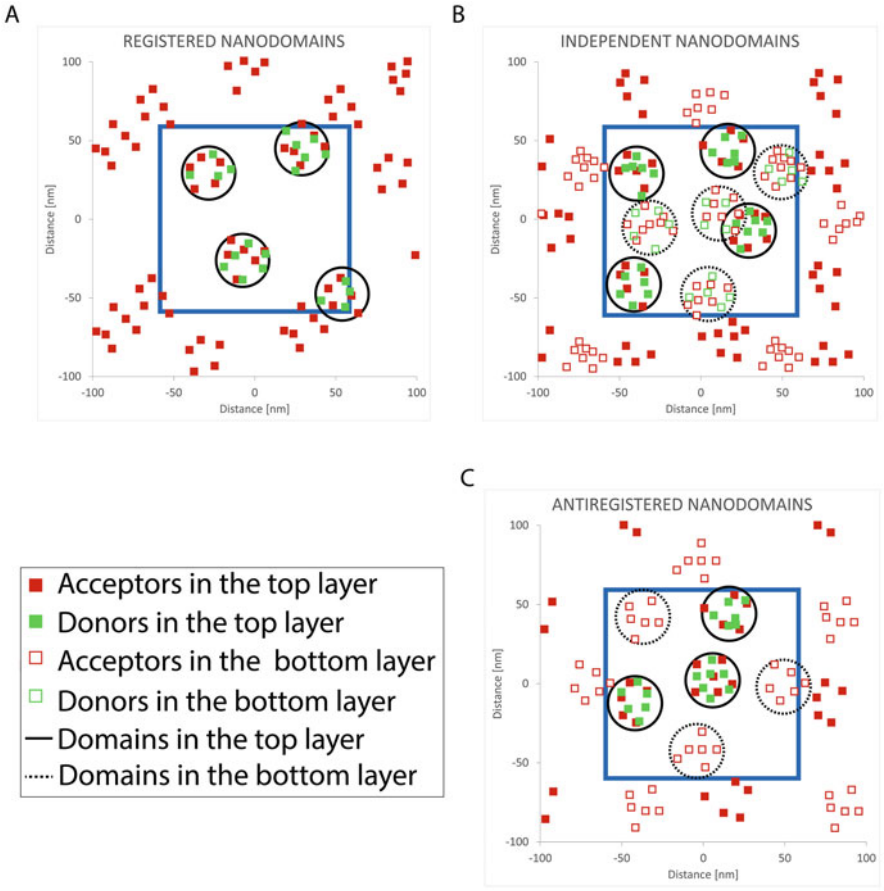

Fig. 4 Schematic planar projection of the simulated lipid bilayer containing: (**a**) perfectly registered; (**b**) independent and (**c**) anti-registered nanodomains. $K_D(D)$, $K_D(A) = 1{,}000$. The blue line indicates the boundaries of the basic simulation box

$$\mathrm{RES} = \frac{1}{n}\sum_{i=1}^{n}\frac{\mathrm{abs}\left(F_{\mathrm{DA,REG}}(t_i) - F_{\mathrm{DA,ANTI/INDEP}}(t_i)\right)}{F_{\mathrm{DA,REG}}(t_i)}100 \tag{9}$$

Thus, RES expresses the difference between the TRF decay for the registered, $F_{\mathrm{DA,\ REG}}(t)$, and either the anti-registered, $F_{\mathrm{DA,\ ANTI}}(t)$, or independent, $F_{\mathrm{DA,\ INDEP}}(t)$, nanodomains.

In analogy to the cases discussed above, the MC-FRET resolution improves, i.e. the RES values increase, as the probe affinity to one of the phases increases (Fig. 5). Case II ($K_D(D) > 1$ and $K_D(A) < 1$) appears again to be the most robust one, exhibiting reasonable resolution for a wide range of $K_D(D/A)$ values. If $K_D(D) = K_D(A)$ (Cases I and III), a higher probe affinity is generally required to

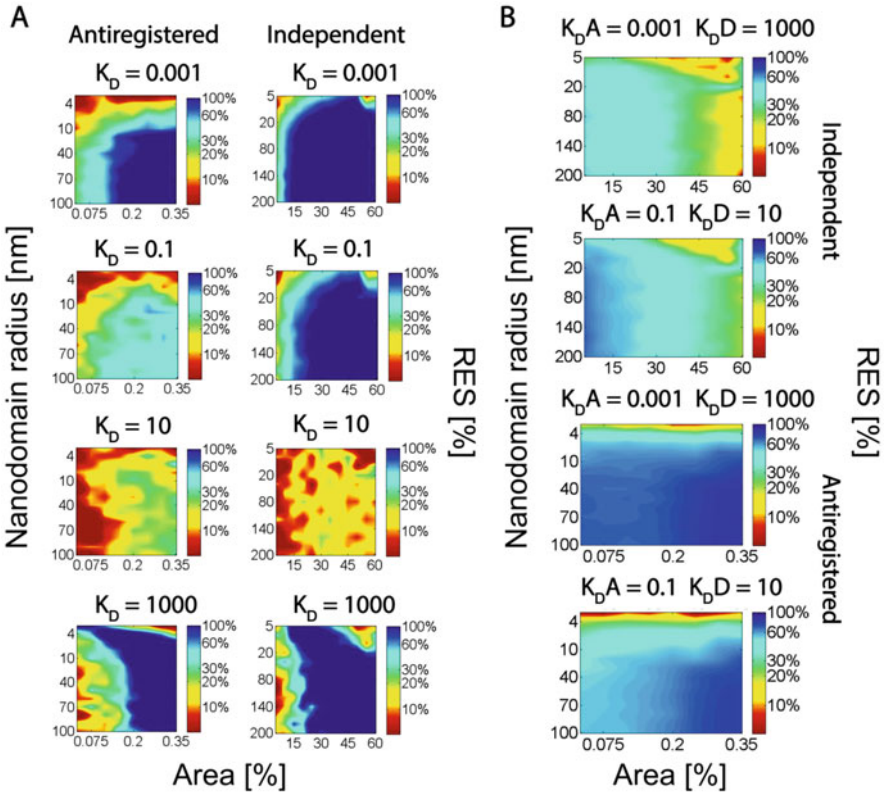

Fig. 5 The potential of MC-FRET to resolve anti-registered/independent from registered nanodomains as a function of the nanodomain radius and the area occupied by the nanodomains. (**a**) $K_D(D) = K_D(A)$, (**b**) $K_D(D) \geq 1$ and $K_D(A) \leq 1$

achieve a similar resolution as for Case II. Both Case I and III achieve the worst resolution for the nanodomains with $\langle R \rangle \leq 7$ nm and $\langle A \rangle \leq 10\%$, which is compensated by a reasonable resolution for the remaining $\langle R \rangle$ and $\langle A \rangle$ if $K_D(D, A) \geq 10$ or $K_D(D, A) \leq 1/10$. Overall, the performed analysis identifies Case I as the worst one, yielding at relatively high $K_D(D/A) = 10$ a relatively low $RES \leq 20$ followed by Case III and Case II. Nevertheless, even the least favourable Case I can be used successfully. In Vinklárek et al. [17] we used headgroup-labelled gangliosides GM_1 ($K_D(D, A) \geq 20$) to provide the first experimental evidence that lipid nanodomains of the sizes between 10 and 160 nm formed at various lipid ratios of 1,2-dioleoyl-sn-glycero-3-phosphocholine (DOPC), cholesterol, sphingomyelin (SM) and oxidized lipids (1-palmitoyl-2-(5′-oxo-valeroyl)-sn-glycero-3-phosphocholine (POVPC) and 1-palmitoyl-2-glutaryl-sn-glycero-3-phosphocholine (PGPC)) are inter-leaflet coupled. Recently, we used the same fluorescent probes to show that GM_1, GM_2 and GM_3 ganglioside nanodomains ($\langle R \rangle \in \langle 7; 120 \rangle$ nm and $\langle A \rangle \in \langle 38; 61 \rangle$ %), with the actual $\langle R \rangle$ and $\langle A \rangle$ parameters depending on the

membrane lipid composition, are also inter-leaflet coupled [25]. Despite these few pieces of evidence, it remains largely unclear to what extent the registration of nanodomains is universal.

3.4 Quantifying Protein Dimerization by MC-FRET

Despite numerous advances in fluorescence lifetime microscopy, characterization of protein interactions in the membranes of living cells by FRET remains challenging. Consequently, affinity parameters such as dissociation constants for membrane protein dimerization are usually obtained only for purified recombinant proteins. They are usually in the form of detergent micelles or at best reconstituted to a simple model membranes. Both the systems are far from the native environment that may also participate in the dimerization.

The ability of FRET to deliver quantitative information is restricted to the bilayers that are perfectly planar, allowing for lateral protein surface concentration to be determined accurately. One of such systems are Giant Plasma Membrane Vesicles (GPMVs). Intrinsically, GPMVs represent a planar membrane system containing varying concentrations of various membrane proteins at the conditions closest to live cells. Quantitative FRET has been used on GPMVs for the first time by Chen and Sarabipour [37, 38]. Below, we are going to show how MC-FRET can be used to quantify protein dimerization in the membranes of GMPVs.

3.4.1 Workflow of MC-FRET for the Quantification of Protein Dimerization

The workflow of an MC-FRET simulation addressing protein–protein interactions is similar to that one previously described for nanodomains (see Sect. 3.2.2). In brief, the protocol requires the information about the concentrations of donor and acceptor labelled proteins, which, as shown later in Sect. 3.4.2, can be obtained directly from an MC-FRET experiment by an initial calibration. In the next step, the initial number of protein monomers and dimers in the simulation box (with the size of $100R_0 \times 100R_0$) is calculated. This is achieved by assuming a starting value of the dissociation constant K_d ($K_d = C^2_{monomer}/C_{dimer}$), where C stands for surface concentrations and the closest protein–protein distance L_0. Afterwards, monomers and dimers are generated on the bilayer surface, and by following the previously described working scheme (see Fig. 2 and Sect. 3.2.2), the simulated decay is computed. K_d and L_0 are optimized until the global minimum in the difference between the measured and simulated TRF decay has been reached. Alternatively, instead of the TRF decays, FRET efficiencies η can be used to optimize K_d and L_0. In this case, η depends on the quantum yields of donors in the presence, Q_{DA}, and absence Q_D of acceptors:

$$\eta = 1 - \frac{Q_{\mathrm{DA}}}{Q_{\mathrm{D}}}, \tag{10}$$

And thus in combination with Eqs. (6) and (7), we get:

$$\frac{Q_{\mathrm{DA}}}{Q_{\mathrm{D}}} = \frac{1}{M} \lim_{M\to\infty} \left(1 + \sum\nolimits_j \left(\frac{R_0}{R_j} \right)^6 \right)^{-1}, \tag{11}$$

And

$$\frac{Q_{\mathrm{DA}}}{Q_{\mathrm{D}}} = \frac{1}{M} \lim_{M\to\infty} \left(1 + \sum\nolimits_j \left(\frac{R_0}{R_{\mathrm{j}}} \right)^6 + 0.5 \times C_2 \times \left(\frac{R_0}{R_{\mathrm{c}}} \right)^4 \right)^{-1}, \text{for } j, \text{where } \left| R_i - R_j \right| \leq 10 R_0. \tag{12}$$

where M runs over all random excitations and over all configurations of the given number of monomers and dimers.

In the case of the TRF decay analysis, measurement on a single GPMV provides us with enough data for the comparison with the simulation. When using efficiencies, number of GPMVs needs to be examined to obtain enough data to be simulated. (How many depends on the precision of the FRET efficiency determination.)

3.4.2 Determination of Donor and Acceptor Surface Concentrations

The success of MC-FRET analysis relies fundamentally on precise determination of the surface concentration of proteins C. More specifically, the analysis requires the following parameters to be determined accurately: (1) the number of membrane proteins in the defined area and (2) the size of that area (to calculate C = number of membrane proteins in the area/the size of that area). In the native cellular membranes, it is almost impossible to determine the latter parameter accurately by fluorescence microscopy, as the membrane forms many inter-membrane contacts, lamellae, etc., which are far beyond optical resolution. Therefore, the work on GPMVs, composition-wise, the closest model system of a native biological membrane that are flat on the micrometre scale, appears inevitable [38]. Yet, it still represents a challenge. In our laboratory, we use fluorescence correlation spectroscopy (FCS) in the way depicted in Fig. 6.

1. *Determination of the number of proteins in the confocal spot*

   FCS allows for very precise determination of the number of molecules in the area illuminated by a tightly focussed laser beam [39]. This can be achieved by measuring temporal autocorrelation functions (ACFs) of the fluctuations in fluorescence intensity, which contain information about the number of fluorescent

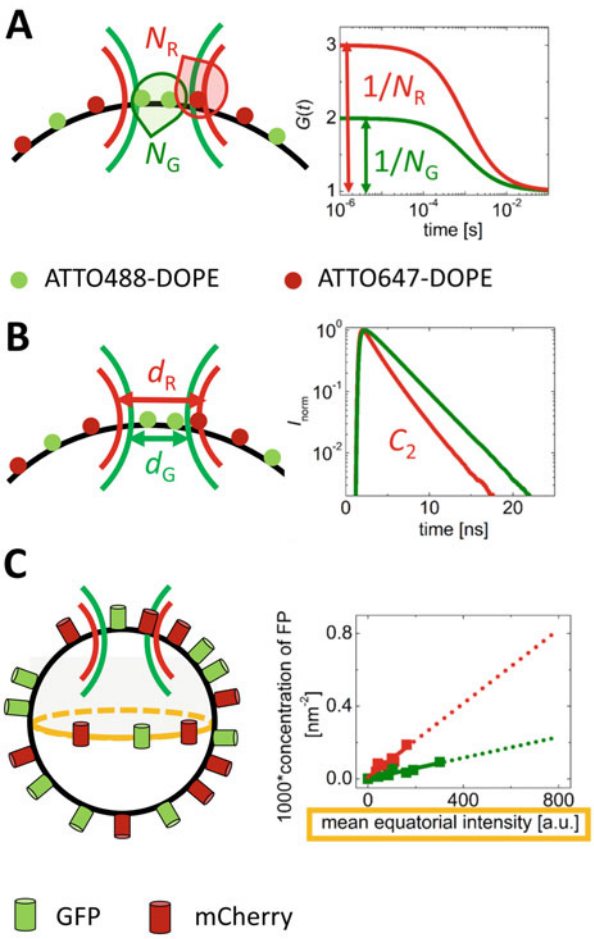

Fig. 6 Determination of the protein surface concentration. (**a**) Determination of the number of fluorescently labelled lipids within the confocal spot by FCS. (**b**) Determination of the surface concentration of homogeneously distributed lipids by FRET. (**c**) Relating mean equatorial fluorescence intensity of fluorescently labelled proteins to their surface concentration

particles (either FP-fused proteins or labelled lipids) and their dynamics in the confocal spot. As shown in Fig. 6a, the amplitudes of ACFs are inversely proportional to the number of diffusing fluorescent particles.

2. *Determination of the size of the confocal spot*

   The profile of the laser light projected on a planar membrane has a 2D Gaussian shape. To estimate the effective size of the beam which FCS counts fluorescent molecules from, one can make use of FRET and Baumann-Fayer model (introduced earlier in Sect. 2) applied to the FRET data acquired in the identical membrane as FCS (ideally the FCS and FRET analysis can be done on the identical dataset). The B.-F. model provides information about the surface concentration of homogeneously distributed, non-interacting acceptors. This concentration can be converted into the FCS-relevant beam size by using information about the number of acceptors in that spot (see step i)). The B.-F. model can be used only for the homogeneously distributed donors and acceptors that in

addition fulfil the requirements on dynamics and isotropy. As this is not the case of FPs, in our laboratory, we determined the effective beam size using a pair of non-interacting headgroup-labelled lipids (ATTO488-DOPE and ATTO647N-DOPE) in a fully artificial system of giant unilamellar vesicles (GUVs) [21]. Overall, this calibration yields the effective diameter of the illuminated area: $d = 0.61 * \frac{\lambda}{N_A}$, where λ stays for the wavelength of the excitation light and N_A is the numerical aperture of the objective (Fig. 6b), and represents a powerful approach that provides geometrical characteristics being fully independent of the used fluorescence moiety.

3. *Determination of protein surface concentrations from equatorial intensity*

   MC-FRET experiments are often performed at high loads of acceptor labelled proteins where FCS cannot be applied. Therefore, as shown on Fig. 6c, it is beneficial to construct a calibration curve for the dependence of the mean equatorial fluorescence intensity on the protein surface concentration. By linear extrapolation of this dependence to higher surface concentrations, one can easily calculate (just by measuring the equatorial intensity without the need to employ FCS for each individual GUV) the protein surface concentration of an examined GPMV. Such a calibration dependence can be acquired either directly on GPMVs by varying the amount of plasmid DNA that encodes the protein of interest used for the transfection of cells, or, alternatively, isolated FPs (without the protein of interest) can be attached to the surface of GUVs doped with DGS-NTA(Ni) lipids via His-tag in large range of surface concentrations.

3.4.3 Dealing with Kappa Squared (κ^2)

The dynamic limit conditions considered so far are based on the assumption that donor and acceptor molecules rotate fast as compared to the donor fluorescence lifetime and their respective transition dipoles can sample the entire rotational space. It is, however, unclear to which extent this stringent assumption holds for barrel-shaped fluorescence proteins attached to the membrane of GPMVs (Fig. 7a, b). The theory of FRET accounting for slow and hindered dipole reorientations is fundamentally different as the distribution of distinct dipole orientations have to be taken into account [22, 40]. Recently, we have shown that, even in this case, the formalism introduced for the dynamic and isotropic regime can be used successfully [21].

Under the dynamic limit conditions, the value of κ^2 equals 2/3. In our work, we optimized the value of κ^2 by correcting the value of experimentally determined R_0 for the used donor–acceptor pair. R_0 depends on κ^2 according to $R_0 \sim \kappa^{\frac{1}{3}}$. Thus, the similarity between the experimentally determined and corrected value ($R_{0,\mathrm{corr}}$) of R_0 reports on to what extent our assumptions about dynamic and isotropic chromophore reorientations hold.

More specifically, we prepared GUVs consisting of POPC and 5 mol% of DGS-NTA(Ni) and attached to them fluorescently labelled fusion proteins containing a His-tag (Fig. 7a, b). We systematically varied the concentration of

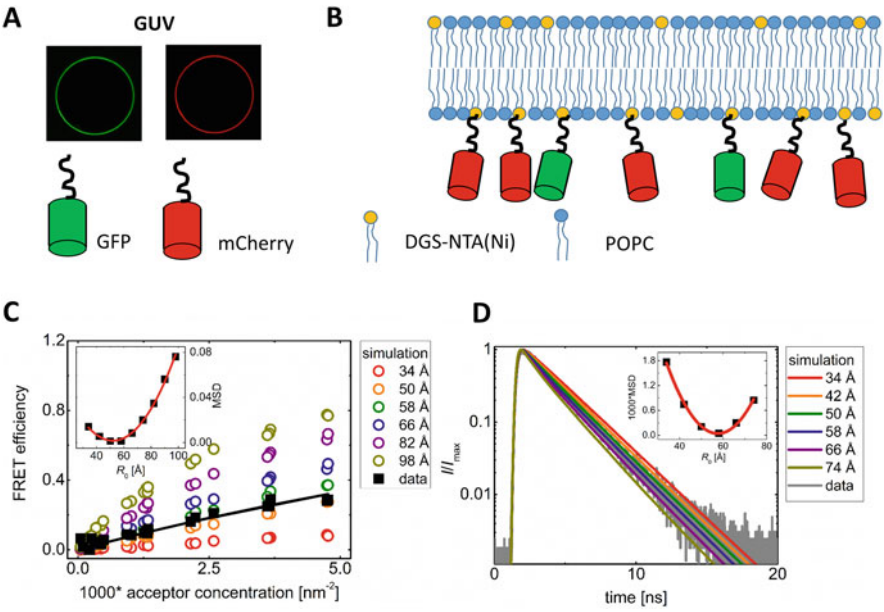

Fig. 7 Determination of the corrected Förster radius, $R_{0,\mathrm{corr}}$. (**a**) Membranes of GUVs with reconstituted GFP (green) and mCherry (red) fluorescent proteins. (**b**) The non-interacting fluorescent proteins are attached to the membrane surface by the bond between DGS-NTA(Ni) (tag in the membrane) and His-tag (tag in the protein). (**c**, **d**) Determination of $R_{0,\mathrm{corr}}$ by measuring (**c**) the efficiency of FRET or (**d**) TRF decays (grey line), respectively, for various concentrations of acceptors. The MC-FRET simulations were carried out for a set of distinct R_0 values and the resulting dependences were compared with the experimental data (in black) by minimizing the mean square displacement (MSD) values (inset)

acceptor proteins while keeping the concentration of donor proteins constant, and we recorded both the TRF decays and the fluorescence intensity in the equatorial plain of GUVs in both fluorescence channels. In this way, we could estimate the surface concentration of donor and acceptor proteins and the efficiency of FRET for each GUV. The efficiency of FRET is estimated by fitting the TFR decays by a sum of exponentials and using the following relationship

$$\eta = 1 - \sum\nolimits_i A_{\mathrm{DA}i}\tau_{\mathrm{DA}i} / \sum\nolimits_i A_{\mathrm{D}i}\tau_{\mathrm{D}i}. \tag{13}$$

Here, ($A_{\mathrm{D}i}$ and $\tau_{\mathrm{D}i}$) or ($A_{\mathrm{DA}i}$ and $\tau_{\mathrm{Da}i}$) are the preexponential factors and individual lifetime components in the absence or presence of acceptors [41].

As shown in Fig. 7c, d, we employed MC-FRET to generate both the FRET efficiencies η and the corresponding donor fluorescence decays F_{DA} for a set of different R_0 and compared those with the experimental data by minimizing the mean square displacement MSD. Whereas in the case of η generation $\mathrm{MSD} = (1/N)\sum_{i=1}^{N}(\eta_{i\ \mathrm{measured}} - \eta_{i\ \mathrm{simulated}})^2$, and i runs over all GUVs that have been

measured, in case of F_{DA} generation $MSD = (1/N)\sum_{i=1}^{N}(F_{DA,i\ measured} - F_{DA,i\ simulated})^2$ and i runs over all TCSPC channels. The best match between the simulated and experimental data was found for $R_{0,corr}$ in the range 50–58 Å. Of note, it was not necessary to optimize the closest distance between the two fluorophores (set to 30 Å) because the range of physically acceptable values was narrow and its impact on the results was insignificant [21].

Interestingly, we performed the experiment for different lengths of the linker between the fusion protein and the His-tag and found that there was no significant dependence of the FRET efficiency on the linker length [21]. The comparison of $R_{0,corr}$ with $R_0 = 52$ Å determined for dynamic isotropic conditions shows that the behaviour of the used donor/acceptor pair is well described by the formalism used. Of course, this does not mean that the chromophores of the investigated proteins behave as fast isotopically rotating dipoles. Instead, it suggests that the herein presented analysis is accurate enough for solving the dimerization issues that are geometrically resembling the system used here. This is of particular importance when protein–protein interactions in the membrane are studied (see the following Sect. 3.4.4).

3.4.4 Dimerizing and Non-dimerizing Membrane Proteins

Figure 8 shows a demonstrative example using two distinct membrane localized proteins: RHBDL2, a human rhomboid protease, which stays in its monomeric form [21, 42] (Fig. 8a), and the human glutamyl carboxypeptidase II (GCPII) that strongly dimerizes in the membrane via its extracellular interface [21, 43] (Fig. 8b). In both the cases, we have co-transfected HeLa cells with eGFP and mCherry fusions to the investigated proteins and formed GPMVs from these cells as described elsewhere [44, 45]. In line with what has been already described in the above paragraphs, we recorded TRF decays and fluorescence intensity in the equatorial plane, estimated the surface concentration of the green and red labelled proteins and performed the MC-FRET analysis.

In this analysis (see also Sect. 3.4.1), either the experimentally determined FRET efficiency measured on an ensemble of GPMVs is fitted to the simulated FRET efficiency (Fig. 8c, e), or, alternatively, an experimental TRF decay is fitted to those generated by MC-FRET (Fig. 8d, f). In both cases, L_0 – the closest protein–protein distance, related to the excluded surface, and K_d – the dissociation constant – were optimized and, importantly, both approaches provided similar results (Fig. 8g, j). While for RHBDL2, we did not see any sign of protein dimerization at the concentrations achievable by overexpression from transfected plasmids, for GCPII, dimers were detected even at the lowest protein surface concentrations used.

Altogether, efforts to characterize membrane proteins by thermodynamic parameters directly in native membranes have been made by us and others. The quantification, however, depends crucially on the determination of lateral protein concentrations. This can be sufficiently done only in limited number of cases as

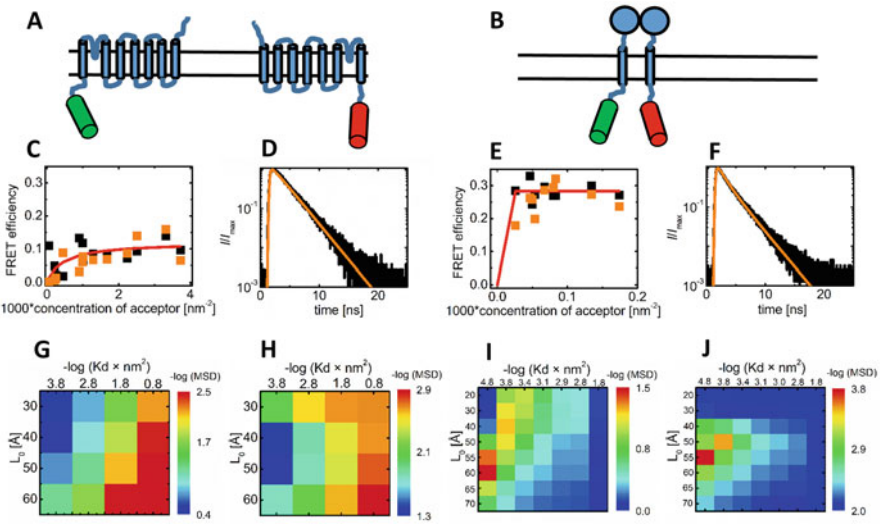

Fig. 8 Quantification of protein dimerization by MC-FRET. (**a**, **b**) A schematic drawing of (**a**) a non-dimerizing protein RHBDL2 and (**b**) a dimerizing protein GCPII. (**c**, **e**) Experimentally determined FRET efficiencies measured on individual GPMVs (black squares) versus FRET efficiencies computed by MC-FRET (orange squares) using as the input simulation parameters the optimal K_d and L_0 values plotted as a function of the acceptor concentration for (**c**) RHBDL2 and (**e**) GCPII. Red line is only intended to guide reader's eyes. (**d**, **f**) An experimental TRF decay (black line) versus a TRF decay generated for the optimal K_d and L_0 parameters (orange line) at given donor/acceptor concentration shown for a selected GPMV containing (**d**) RHBDL2 or (**f**) GCPIIGCPII, respectively. (**g**–**j**) MSD maps (i.e. 2D plots of MSD as a function K_d and L_0 parameters) generated by MC-FRET for the GPMVs containing (**g**, **h**) RHBDL2 or (**i**, **j**) GCPIIGCPII, respectively. MSD was calculated both by means of the FRET efficiencies (panels **g** and **i**) and TRF decays (panels **h** and **j**; see also the text for more details)

even the plasma membrane turns out to be too ruffled for area determination. Eventually, the experiments had to be carried out in GPMVs, model membranes that are compositionally closest to the native ones. These attempts however revealed important considerations that have to be made when membrane protein oligomerization is addressed even if the quantification is not the main goal. Firstly, as the FRET read-out is almost always present in the 2D systems, a negative control of a similar acceptor expression is essential for drawing conclusions. Secondly, the membrane attached FPs behave as if they were in the isotropic, dynamic regime. Moreover, we do not see any linker length dependence. Therefore, in planning the FRET experiment, there is no need to be overwhelmingly cautious about these aspects.

4 Conclusions

In summary, recent advances in fluorescence microscopy and spectroscopy have enabled to characterize organization of lipids and proteins in plasma membranes and their models with great spatiotemporal resolution. One of these techniques is the recently developed MC-FRET method, which can, by using standard fluorescence lifetime microscopy equipment and analysis tools based on Monte-Carlo simulations, (1) detect nanoscopic heterogeneities formed in lipid bilayers, (2) determine their sizes with the sensitivity down to only a few nanometres in radius, (3) quantify their membrane surface coverage and (4) characterize their mutual inter-leaflet organization. Moreover, it can also be used to study protein dimerization in the membrane by quantifying the dissociation constant for dimerization. Overall, the method reaches a nanometre resolution in all three directions, and thus offers an effective tool in the field of membrane biophysics.

Acknowledgements RŠ and BC acknowledge GAČR Grant 20-01401J. JH would like to acknowledge the support of the Czech Science Foundation by grant number 19-18917S. KS would like to acknowledge the Czech Science Foundation (grant number 18-09556S), and Operational Programme European Regional Development Fund (project no. CZ.02.1.01/0.0/0.0/16_019/0000729). BC would like to acknowledge Project No. SVV 260586 of the Charles University.

References

1. Bernardino de la Serna J, Schütz GJ, Eggeling C, Cebecauer M (2016) There is no simple model of the plasma membrane organization. Front Cell Dev Biol 4(September):1–17
2. Cebecauer M, Amaro M, Jurkiewicz P, Sarmento MJ, Šachl R, Cwiklik L et al (2018) Membrane lipid nanodomains. Chem Rev 118(23):11259–11297
3. Sarmento MJ, Ricardo JC, Amaro M, Šachl R (2020) Organization of gangliosides into membrane nanodomains. FEBS Lett 594(22):3668–3697. https://doi.org/10.1002/1873-3468.13871
4. Shi J, Yang T, Kataoka S, Zhang Y, Diaz AJ, Cremer PS (2007) GM1 clustering inhibits cholera toxin binding in supported phospholipid membranes. J Am Chem Soc 129(18):5954–5961
5. Sarmento MJ, Coutinho A, Fedorov A, Prieto M, Fernandes F (2014) Ca2 + induces PI(4,5)P2 clusters on lipid bilayers at physiological PI(4,5)P2 and Ca2 + concentrations. Biochim Biophys Acta Biomembr 1838(3):822–830
6. Sarmento MJ, Coutinho A, Fedorov A, Prieto M, Fernandes F (2017) Membrane order is a key regulator of divalent cation-induced clustering of PI(3,5)P2 and PI(4,5)P2. Langmuir 33(43):12463–12477
7. Sjöholm J, Bergstrand J, Nilsson T, Šachl R, Von Ballmoos C, Widengren J et al (2017) The lateral distance between a proton pump and ATP synthase determines the ATP-synthesis rate. Sci Rep 7(April):1–12
8. Koukalová A, Amaro M, Aydogan G, Gröbner G, Williamson PTF, Mikhalyov I et al (2017) Lipid driven nanodomains in giant lipid vesicles are fluid and disordered. Sci Rep 7(1):5460. http://www.nature.com/articles/s41598-017-05539-y
9. Betzig E, Patterson GH, Sougrat R, Lindwasser OW, Olenych S, Bonifacino JS et al (2006) Imaging intracellular fluorescent proteins at nanometer resolution. Science 313(5793):1642–1645

10. Rust MJ, Bates M, Zhuang X (2006) Sub-diffraction-limit imaging by stochastic optical reconstruction microscopy (STORM). Nat Methods 3(10):793–795
11. Hell SW, Wichmann J (1994) Breaking the diffraction resolution limit by stimulated emission: stimulated-emission-depletion fluorescence microscopy. Opt Lett 19(11):780
12. Piliarik M, Sandoghdar V (2014) Direct optical sensing of single unlabelled proteins and super-resolution imaging of their binding sites. Nat Commun 5(1):1–8
13. Young G, Hundt N, Cole D, Fineberg A, Andrecka J, Tyler A et al (2018) Quantitative mass imaging of single biological macromolecules. Science 360(6387):423–427
14. Owen DM, Magenau A, Williamson D, Gaus K (2012) The lipid raft hypothesis revisited - new insights on raft composition and function from super-resolution fluorescence microscopy. BioEssays 34(9):739–747
15. Cheng X, Smith JC (2019) Biological membrane organization and cellular signaling. Chem Rev 119(9):5849–5880
16. Šachl R, Johansson LB, Hof M (2012) Förster resonance energy transfer (FRET) between heterogeneously distributed probes: application to lipid nanodomains and pores. Int J Mol Sci 13(12):16141–16156
17. Vinklárek IS, Vel'As L, Riegerová P, Skála K, Mikhalyov I, Gretskaya N et al (2019) Experimental evidence of the existence of interleaflet coupled nanodomains: an MC-FRET study. J Phys Chem Lett 10(9):2024–2030
18. Šachl R, Humpolíčková J, Štefl M, Johansson LB, Hof M (2011) Limitations of electronic energy transfer in the determination of lipid nanodomain sizes. Biophys J 101(11):L60-2
19. King C, Sarabipour S, Byrne P, Leahy DJ, Hristova K (2014) The FRET signatures of noninteracting proteins in membranes: simulations and experiments. Biophys J 106(6): 1309–1317. https://doi.org/10.1016/j.bpj.2014.01.039
20. King C, Raicu V, Hristova K (2017) Understanding the FRET signatures of interacting membrane proteins. J Biol Chem 292(13):5291–5310
21. Škerle J, Humpolíčková J, Johnson N, Rampírová P, Poláchová E, Fliegl M et al (2020) Membrane protein dimerization in cell-derived lipid membranes measured by FRET with MC simulations. Biophys J 118(8):1861–1875
22. Baumann J, Fayer MD (1986) Excitation transfer in disordered two-dimensional and anisotropic 3-dimensional systems - effects of spatial geometry on time-resolved observables. J Chem Phys 85(7):4087–4107
23. Šachl R, Boldyrev I, Johansson LB (2010) Localisation of BODIPY-labelled phosphatidylcholines in lipid bilayers. Phys Chem Chem Phys 12(23):6027–6034
24. Amaro M, Šachl R, Aydogan G, Mikhalyov II, Vácha R, Hof M (2016) GM1 ganglioside inhibits b-amyloid oligomerization induced by sphingomyelin. Angew Chemie 55:9411–9415
25. Sarmento MJ, Owen MC, Ricardo JC, Chmelová B, Davidović D (2021) The impact of the glycan headgroup on the nanoscopic segregation of gangliosides. Biophys J 120:5530–5543
26. Loura LMS, Fedorov A, Prieto M (2001) Exclusion of a cholesterol analog from the cholesterol-rich phase in model membranes. Biochim Biophys Acta Biomembr 1511(2):236–243
27. Loura LMS, Fedorov A, Prieto M (2000) Partition of membrane probes in a gel/fluid two-component lipid system: a fluorescence resonance energy transfer study. Biochim Biophys Acta Biomembr 1467(1):101–112
28. Buboltz JT (2007) Steady-state probe-partitioning FRET: a simple and robust tool for the study of membrane phase behavior. Phys Rev E 76:021903
29. Charron DM, Zheng G (2018) Nanomedicine development guided by FRET imaging. Nano Today 18:124–136
30. Silva LC, De Almeida RFM, Castro BM, Fedorov A, Prieto M (2007) Ceramide-domain formation and collapse in lipid rafts: membrane reorganization by an apoptotic lipid. Biophys J 92(2):502–516. https://doi.org/10.1529/biophysj.106.091876
31. Enoki TA, Heberle FA, Feigenson GW (2018) FRET detects the size of nanodomains for coexisting liquid-disordered and liquid-ordered phases. Biophys J 114(8):1921–1935. https://doi.org/10.1016/j.bpj.2018.03.014

32. Bordovsky SS, Wong CS, Bachand GD, Stachowiak JC, Sasaki DY (2016) Engineering lipid structure for recognition of the liquid ordered membrane phase. Langmuir 32(47):12527–12533
33. Štefl M, Šachl R, Humpolíčková J, Cebecauer M, MacHáň R, Kolářová M et al (2012) Dynamics and size of cross-linking-induced lipid nanodomains in model membranes. Biophys J 102(9):2104–2113
34. De Almeida RFM, Loura LMS, Fedorov A, Prieto M (2005) Lipid rafts have different sizes depending on membrane composition: a time-resolved fluorescence resonance energy transfer study. J Mol Biol 346(4):1109–1120
35. Usery RD, Enoki TA, Wickramasinghe SP, Nguyen VP, Ackerman DG, Greathouse DV et al (2018) Membrane bending moduli of coexisting liquid phases containing transmembrane peptide. Biophys J 114(9):2152–2164. https://doi.org/10.1016/j.bpj.2018.03.026
36. Sarmento MJ, Hof M, Šachl R (2020) Interleaflet coupling of lipid nanodomains – insights from in vitro systems. Front Cell Dev Biol 8:284
37. Chen L, Novicky L, Merzlyakov M, Hristov T, Hristova K (2010) Measuring the energetics of membrane protein dimerization in mammalian membranes. J Am Chem Soc 132(10): 3628–3635
38. Sarabipour S, Nuala DP, Hristova K (2015) Characterization of membrane protein interactions in plasma membrane derives vesicles with quantitative imaging fret. Acc Chem Res 48(8): 2262–2269
39. Benda A, Beneš M, Mareček V, Lhotský A, Hermens WT, Hof M (2003) How to determine diffusion coefficients in planar phospholipid systems by confocal fluorescence correlation spectroscopy. Langmuir 19(10):4120–4126
40. Engström S, Lindberg M, Johansson LB (1988) Monte Carlo simulations of electronic energy transfer in three-dimensional systems: a comparison with analytical theories. J Chem Phys 89(1):204–213
41. Becker W (2012) Fluorescence lifetime imaging - techniques and applications. J Microsc 247(2):119–136
42. Kreutzberger AJB, Urban S (2018) Single-molecule analyses reveal rhomboid proteins are strict and functional monomers in the membrane. Biophys J 115(9):1755–1761
43. Schülke N, Varlamova OA, Donovan GP, Ma D, Gardner JP, Morrissey DM et al (2003) The homodimer of prostate-specific membrane antigen is a functional target for cancer therapy. Proc Natl Acad Sci U S A 100(22):12590–12595
44. Del Piccolo N, Placone J, He L, Agudelo SC, Hristova K (2012) Production of plasma membrane vesicles with chloride salts and their utility as a cell membrane mimetic for biophysical characterization of membrane protein interactions. Anal Chem 84(20):8650–8655
45. Sezgin E, Kaiser HJ, Baumgart T, Schwille P, Simons K, Levental I (2012) Elucidating membrane structure and protein behavior using giant plasma membrane vesicles. Nat Protoc 7(6):1042–1051. https://doi.org/10.1038/nprot.2012.059